

PAPER • OPEN ACCESS

Measurement of the tilt angle of turbulent structures in magnetically confined plasmas using Doppler reflectometry

To cite this article: J R Pinzón *et al* 2019 *Plasma Phys. Control. Fusion* **61** 105009

View the [article online](#) for updates and enhancements.

Recent citations

- [A theoretical investigation of the turbulent structures tilting measurements with radial correlation Doppler reflectometry](#)
O L Krutkin *et al*



IOP | ebooks™

Bringing you innovative digital publishing with leading voices to create your essential collection of books in STEM research.

Start exploring the collection - download the first chapter of every title for free.

Measurement of the tilt angle of turbulent structures in magnetically confined plasmas using Doppler reflectometry

J R Pinzón^{1,2,5} , T Estrada³, T Happel¹ , P Hennequin⁴ , E Blanco³,
U Stroth^{1,2}, the ASDEX Upgrade¹ and TJ-II Teams³

¹Max-Planck-Institute für Plasmaphysik, Garching, Germany

²Physics Department E28, TUM, D-85748, Garching, Germany

³Laboratorio Nacional de Fusión, CIEMAT, Madrid, Spain

⁴Laboratoire de Physique de Plasmas, Ecole Polytechnique, Palaiseau, France

E-mail: javier.pinzon@ipp.mpg.de

Received 9 May 2019, revised 17 July 2019

Accepted for publication 7 August 2019

Published 4 September 2019



CrossMark

Abstract

The mean tilt angle of turbulent structures is a key element for describing the turbulence and its interplay with plasma flows in magnetically confined plasmas. It is a quantity predicted by theories and gyrokinetic simulations, which can provide information on the type of the dominant micro-instability, and also on the turbulence anisotropy induced by sheared flows. A new method for measuring the tilt angle of turbulent structures using Doppler reflectometry has been recently introduced (Pinzón *et al* 2019 *Nucl. Fusion* **59** 074002). It is based on the time delay of the cross-correlation between microwaves backscattered at radially displaced positions. In this paper, the method is presented in detail and is successfully applied on the ASDEX Upgrade tokamak and the TJ-II stellarator. Measurements of the tilt angle in the core of both machines are reported, in the TJ-II case, for the first time.

Keywords: plasma turbulence, plasma diagnostics, Doppler reflectometry

(Some figures may appear in colour only in the online journal)

1. Introduction

Turbulence contributes significantly to the transport of energy and particles in magnetically confined plasmas, limiting the energy confinement time and thus the plasma performance in experiments. Accordingly, the understanding of turbulence dynamics in fusion plasmas is important for optimizations of present experiments and design of future fusion reactors [1]. Recent developments of theoretical models and gyrokinetic simulations have made detailed predictions of turbulence

properties possible [2–4]. However, this progress has to be accompanied by exhaustive comparisons with fluctuation measurements, which are fundamental for the validation of models and codes [5–8]. Improvements of fluctuation diagnostics have enabled comprehensive comparisons that have contributed to a better understanding of specific aspects of turbulence and transport in experiments [9–11]. Nevertheless, despite of the large progress in this field, more detailed fluctuation measurements are still required for comparisons of specific aspects.

The turbulent fluctuations of the plasma parameters, in particular the electron density n , lead to the formation of *turbulent structures* or *eddies*. Given the complexity of fusion plasmas characterized by strong magnetic fields, the radial variation of the plasma parameters and sheared plasma flows, turbulence is not isotropic. Accordingly turbulent structures are elongated and tilted. The mean structure tilt indicates the turbulence anisotropy which is a relevant ingredient commonly

⁵ Author to whom any correspondence should be addressed.



Original content from this work may be used under the terms of the [Creative Commons Attribution 3.0 licence](https://creativecommons.org/licenses/by/3.0/). Any further distribution of this work must maintain attribution to the author(s) and the title of the work, journal citation and DOI.

invoked in theories and models. The tilt is a key parameter for characterizing the interaction between turbulence and plasma flows constituting a strongly coupled system [12–14]. Turbulence can excite flows via the Reynolds stress mechanism, which requires elongated and systematically tilted turbulent structures [15, 16]. Complementary, sheared flows can tilt and stretch structures leading to a reduction of the turbulence level [17, 18]. The micro-instabilities responsible for driving turbulence have a *global structure* which is tilted depending on the radial shearing of the plasma parameters [19, 20].

The fast dynamics of particles along the magnetic field \mathbf{B} smooths out fluctuation in this direction, hence in this paper, turbulent structures are described on the radial-perpendicular plane. As usual, the radial (r) direction is defined normal to the magnetic flux surfaces, and the perpendicular (\perp) direction is tangential to the flux surfaces and perpendicular to the magnetic field \mathbf{B} . The *tilt angle of turbulent structures* θ_{turb} is defined with respect to the radial direction.

The tilt angle is a quantity predicted by theories and simulations. In [17] and [19], an estimate of the tilt angle was obtained using the *linear ballooning theory*, which showed the dependence of the tilt angle on the radial profiles of plasma parameters and on the $E \times B$ flow shear. In [20], differences of the tilt angle were found using global gyrokinetic simulations for different types of dominant micro-instabilities, e.g. the ion-temperature-gradient or the trapped-electron modes. Moreover, in the same reference the role of the tilt angle in determining the residual stress contribution to momentum transport was demonstrated with fluid models. In [21], the experimentally obtained intrinsic toroidal rotation on the ASDEX Upgrade tokamak was reproduced by including a finite tilt angle in local gyrokinetic simulations.

Despite of the strong physical interest in the tilt angle, its direct measurement remains challenging, especially in the confined region of fusion plasmas. The tilt of turbulent structures was measured in the scrape-off layer using gas puff imaging [22, 23], Langmuir probes [24, 25] and beam emission spectroscopy [26, 27]. Recently, a new method for measuring the tilt angle of turbulent structures was introduced [28]. It is based on Doppler reflectometry and therefore, is non-invasive and applicable in the core region of fusion plasmas, where it was used to demonstrate the effect of sheared $E \times B$ flows in different turbulence regimes. In this paper, the new technique is presented in detail and its applicability to general experimental conditions is discussed. Furthermore, the method is applied on the ASDEX Upgrade tokamak and on the TJ-II stellarator. Measurements of the tilt angle in the core region of both machines are provided.

Doppler reflectometry is an established diagnostic technique used for the characterization of density fluctuations and flows in magnetic confined plasmas [29–34]. It uses an obliquely injected microwave beam which propagates in the plasma and is reflected at the so-called cutoff layer, where the electric field of the microwave is maximum and hence backscattering at density fluctuations is strong. This provides the diagnostic with a good spatial localization of measurements at perpendicular wavenumber k_{\perp} fulfilling the Bragg condition, $k_{\perp} = -2k_i$ where k_i is the wavenumber of the

probing wave at the cutoff. The frequency Doppler shift f_D of the backscattered signal provides the perpendicular velocity of density fluctuations

$$u_{\perp} = \frac{2\pi f_D}{k_{\perp}}, \quad (1)$$

which is a combination of the $E \times B$ drift and the turbulence phase velocities; $u_{\perp} = u_{E \times B} + v_{\text{ph}}$. Furthermore, the backscattered power gives information on the k_{\perp} resolved fluctuation level. It has been shown that for low turbulence levels, in the so-called *linear regime*, the signal is proportional to the fluctuation amplitude [35]; whereas for large fluctuation levels, multiple scattering events introduce deviations in the so-called *nonlinear regime* [36, 37].

The radial structure of the density fluctuations has been investigated by using two microwave beams probing at radially displaced positions. The probing frequency of one beam (referred to as the *reference channel*) is fixed keeping a constant measurement position, while the frequency of the other (*hopping channel*) is scanned, producing a radial variation of the measurement position. In this technique, often called radial correlation Doppler reflectometry [38–40], the correlation level of the two reflectometer channels is analysed as a function of the radial separation of the measurement positions Δr . The 1/e-decay length is used as an estimate of the radial correlation length L_r of the density fluctuations.

The cross-correlation function between the Doppler reflectometer signals is:

$$C_{\Delta r}(\tau) = \frac{\int dt (V_{\text{ref}}(t) - \langle V_{\text{ref}} \rangle)(V_{\text{hop}}(t + \tau) - \langle V_{\text{hop}} \rangle)^*}{\sqrt{\int dt |V_{\text{ref}}(t) - \langle V_{\text{ref}} \rangle|^2 \int dt |V_{\text{hop}}(t) - \langle V_{\text{hop}} \rangle|^2}}, \quad (2)$$

where $V_{\text{ref/hop}}$ is the reflectometer signal of the reference/hopping channel and τ is the time lag of the cross-correlation. $\langle \cdot \rangle$ stands for the time average and $*$ means complex conjugate. The dependence on the radial separation Δr has been explicitly written. In the standard radial correlation technique, the maximum of $C_{\Delta r}(\tau)$ is regarded for estimations of L_r [38, 39]. In the present paper, the *time delay* τ_{max} at maximum cross-correlation and geometrical considerations are used in order to provide a measurement of the tilt angle of the turbulent structures.

This paper is organized as follows: in section 2 the measurement method of the tilt angle is developed for a synthetic turbulent field and assuming a simplified diagnostic response. Diagnostic effects on the tilt angle measurement are discussed at the end of the section. In section 3 the influence of the temporal decorrelation of the turbulence is discussed; an associated correction factor important for interpretation of experimental data is derived. In sections 4 and 5 the method is applied on the ASDEX Upgrade tokamak and on the TJ-II stellarator, respectively. In section 6 the summary is presented.

2. Measurement method

The method for measuring the tilt angle of turbulent structures is presented in slab geometry and for synthetic turbulence. In

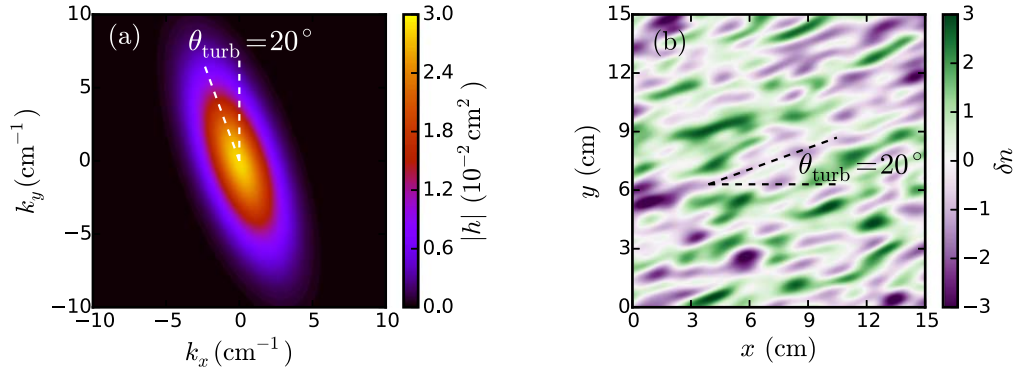


Figure 1. (a) Two-dimensional wavenumber spectrum $h(k_x, k_y)$ from equation (3) and (b) a sample of the turbulence field $\delta n(x, y)$ for $\ell_{\max} = 1.40$ cm, $\ell_{\min} = 0.51$ cm and $\theta_{\text{turb}} = 20^\circ$. Elongated and tilted turbulent structures are obtained.

slab geometry the Cartesian coordinates x , y and z are related to the radial, perpendicular and magnetic field directions in fusion plasmas, respectively. The slab geometry is a local approximation to fusion plasmas commonly used for modelling and simulation of Doppler reflectometry [37, 41]. A two-dimensional turbulence with a Gaussian wavenumber spectrum is considered. It produces elongated and tilted structures. In this section, the tilt angle is obtained from the time delay of the cross-correlation function of Doppler reflectometry measurements. A simplified diagnostic response is assumed, though geometrical effects of the beam propagation are considered. At the end of the section, further diagnostic effects are discussed.

2.1. Turbulence model

Gaussian spectra are commonly used in theory [36, 41] and simulations [37, 42] of Doppler reflectometry. They exhibit a spectral decay with the wavenumber as qualitatively expected for real turbulence, are suitable for analytical calculations, and produce turbulent fields with well defined statistical properties.

Given the fast dynamics along the magnetic field, turbulence is defined on the x and y coordinates in the slab case. Accordingly, the wavenumber spectrum is defined on the k_x and k_y coordinates. In order to include anisotropy in the model, a two-dimensional elongated and tilted Gaussian spectral amplitude is chosen:

$$|h(k_x, k_y)| = \frac{\ell_{\min} \ell_{\max}}{4\pi} \times \exp\left[-\frac{(k_x \cos \theta_{\text{turb}} + k_y \sin \theta_{\text{turb}})^2 \ell_{\max}^2}{8}\right] \times \exp\left[-\frac{(k_x \sin \theta_{\text{turb}} - k_y \cos \theta_{\text{turb}})^2 \ell_{\min}^2}{8}\right], \quad (3)$$

where θ_{turb} gives the tilt of the spectrum with respect to the k_y -axis, and ℓ_{\max} and ℓ_{\min} are lengths that define the spectral widths. The physical meaning of these lengths and the complex phase of h will be discussed below. The contour plot of $|h|$ for $\ell_{\max} = 1.40$ cm, $\ell_{\min} = 0.51$ cm and $\theta_{\text{turb}} = 20^\circ$ is shown in figure 1(a). Elongation and tilt can be recognized.

This type of wavenumber spectrum has been used in [37] for investigations of the linearity of Doppler reflectometry measurements.

The turbulent field of density fluctuations $\delta n(x, y)$ is the inverse Fourier transform of $h(k_x, k_y)$:

$$\delta n(x, y) = \iint dk_x dk_y h(k_x, k_y) e^{ik_x x + ik_y y}. \quad (4)$$

For the analytical calculations, all the integrals are performed over the range $(-\infty, \infty)$. For numerical applications the turbulent field $\delta n(x, y)$ is computed by a 2D fast Fourier transform of $h(k_x, k_y)$ over a finite domain after including random phases ϕ :

$$h(k_x, k_y) = |h(k_x, k_y)| e^{i\phi(k_x, k_y)}. \quad (5)$$

The resulting turbulent field is dimensionless and has a rms value of 1; moreover its mean value has been set to zero. This normalization is convenient for the following correlation analysis, nevertheless other normalizations can be used in order to include the turbulence level and proper physical dimensions [37].

A sample contour plot of the turbulent field is shown in figure 1(b) for the wavenumber spectrum from figure 1(a). Elongated and tilted turbulent structures can be observed. On average, the structures are tilted by $\theta_{\text{turb}} = 20^\circ$ with respect to the x -axis. The average size along the major and minor axes is ℓ_{\max} and ℓ_{\min} , respectively. It will be shown next that these two quantities correspond to the widths of the correlation function along the principal axes. The ratio ℓ_{\max}/ℓ_{\min} defines the elongation of the turbulent structures, which for the depicted case is 2.745.

2.2. Cross-correlation function

Here the turbulent field is characterized assuming its local (point like) measurement. This is a reasonable approximation to Doppler reflectometry measurements given their good spatial localization, moreover it is suitable for developing the method. The reflectometer signal when probing at (x, y) is taken proportional (linear) to the density fluctuation amplitude at the measurement position

$$V(x, y) = \delta n(x, y). \quad (6)$$

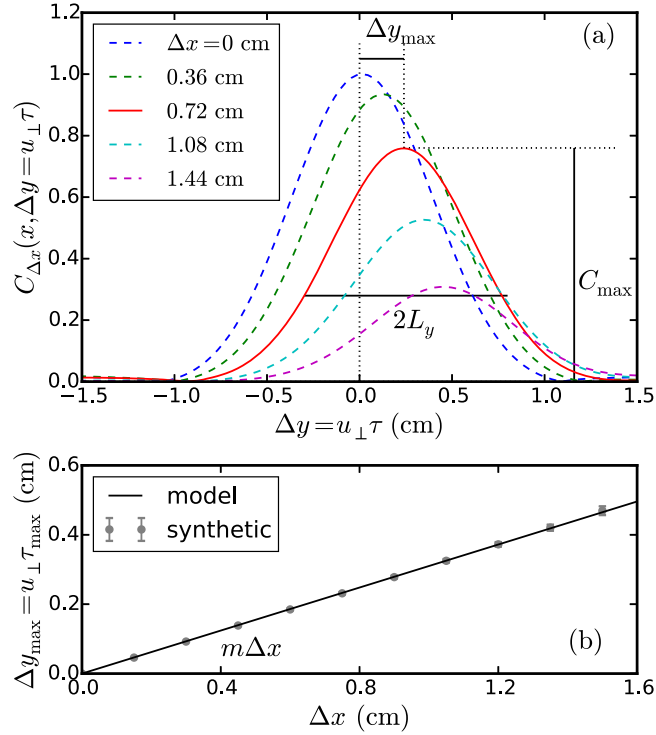


Figure 2. (a) Cross-correlation function $C_{\Delta x}(x, \Delta y)$ for different separations Δx . The definitions of C_{\max} , L_y and Δy_{\max} are illustrated. (b) Position of the maximum of the cross-correlation Δy_{\max} as a function of the separation Δx . The slope m is indicated. The solid line depicts the analytical results from equation (14).

Diagnostic effects related to the finite scattering volume, contributions different from the cutoff, and a nonlinear response will be discussed at the end of the section.

The turbulence advection by perpendicular plasma flows results in a time dependence of the reflectometer signals. Since the perpendicular velocity u_{\perp} is held constant, it provides the equivalence $y = u_{\perp} t$ that allows to link directly the y -coordinate to time. Thus the y -dependence of δn is equivalent to a time dependence of the reflectometer signal. The previous relationship assumes the turbulence *frozen* in the plasma frame neglecting any intrinsic dynamics of the turbulence. Deviations from the frozen turbulence will be discussed in section 3.

Following equation (2), the cross-correlation function of the reference and hopping channels probing at x and $x + \Delta x$, respectively, is

$$C_{\Delta x}(x, \Delta y) = \int dy \delta n^*(x, y) \delta n(x + \Delta x, y + \Delta y). \quad (7)$$

An appropriated normalization of the turbulent field is chosen such that no denominator is required. Given the frozen turbulence approximation, the displacement Δy is translated into the time lag of the cross-correlation $\tau = \Delta y / u_{\perp}$.

The cross-correlation function is computed for the synthetic turbulent field shown in figure 1(b) at an arbitrary x position. The results are plotted in figure 2(a) for several separations of the channels Δx in different colours. In all cases a peak is observed, which decreases and moves to positive Δy values when Δx increases. The correlation

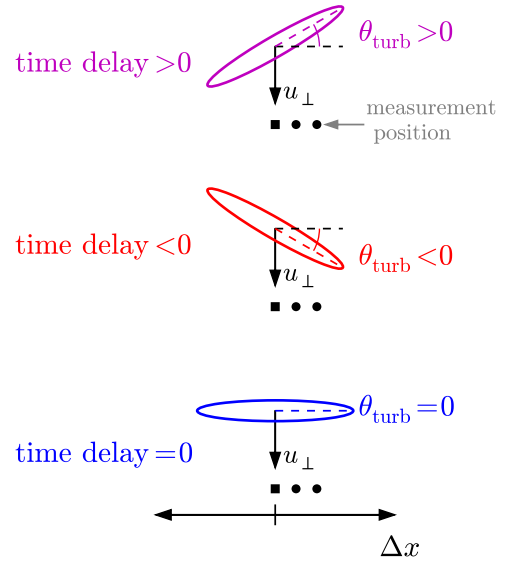


Figure 3. Schematics illustrating the effect of tilted turbulent structures propagating with velocity u_{\perp} on the time delay.

function is characterized with its maximum C_{\max} , position of the maximum Δy_{\max} , and width L_y . The three quantities are indicated in figure 2(a) for the $\Delta x = 0.72$ cm curve in red. Note that $C_{\Delta x=0}(x, \Delta y)$ (blue) is the autocorrelation function.

The decrease of the correlation level C_{\max} with Δx is due to the spatial decorrelation of the turbulence in the x direction. Commonly, radial correlation Doppler reflectometry analyses the dependence of C_{\max} on Δx for estimating the radial correlation length of the turbulence [38, 39, 42]. In contrast, this paper investigates the *time delay* between the signals defined as $\tau_{\max} = \Delta y_{\max} / u_{\perp}$ for measuring the tilt angle of the turbulent structures.

Figure 2(b) shows the position of the maximum correlation Δy_{\max} (or equivalently the time delay) as a function of Δx . Symbols depict the results from the synthetic turbulence and the error bars indicate the standard deviation when considering different reference positions x . The solid line depicts an analytical prediction which will be discussed later. Δy_{\max} shows a linear behaviour $\Delta y_{\max} = m\Delta x$ characterized with a slope m .

The linear behaviour of Δy_{\max} or of the time delay is induced by the tilt angle of the turbulent structures. This is schematically shown in figure 3 where three schematic structures with different tilt angles are displayed. The measurement points are depicted by black symbols, the square indicates the reference. A counter-clockwise tilted structure (purple) is seen earlier by the reference channel, resulting in a positive time delay that increases with Δx , and gives a positive slope m . On the contrary, a clockwise tilted structure (red) is seen later by the reference channel giving a negative time delay and m value. If the structure is not tilted and therefore aligned with the measurement points, the time delay and m are zero.

Radial propagation of the turbulent structures (propagation in the x -direction in slab geometry) would introduce further contributions to the time delay not related to the tilt angle. Nevertheless the main dynamics of the turbulence

occurs in the perpendicular direction and is given by the $E \times B$ and phase velocities [29, 43, 44]. Even if structures propagate radially, only minor corrections to the time delays are expected as long as the radial velocity is much smaller than the perpendicular one. This condition will be further discussed based on experimental results in section 4.2.

2.3. Quantitative relationship between tilt angle and time delay

In order to relate numerically the slope m (see figure 2(b)) to the turbulence characteristics and in particular to the tilt angle θ_{turb} , the cross-correlation function is analytically computed for the wavenumber spectrum of equation (3).

For the following analytical calculations it is suitable to integrate equation (7) along x :

$$C_{\Delta x}(\Delta y) = \iint dx dy \delta n^*(x, y) \delta n(x + \Delta x, y + \Delta y). \quad (8)$$

Its results are equivalent to those of equation (7) for a statistically homogeneous turbulent field. Moreover, it is convenient because it provides the 2D correlation function of the turbulent field.

Inserting equation (4) into (8) yields the correlation function of turbulence with wavenumber spectrum h :

$$C_{\Delta x}(\Delta y) = \iint dk_x dk_y |h(k_x, k_y)|^2 e^{ik_x \Delta x + ik_y \Delta y}, \quad (9)$$

which corresponds to the inverse Fourier transform of $|h|^2$. Equation (9) allows to link quantitatively the characteristics of the correlation function to the wavenumber spectrum of the turbulence.

The correlation function of the Gaussian wavenumber spectrum in equation (3) is computed using equation (9). In this case a 2D Gaussian is obtained,

$$C_{\Delta x}(\Delta y) = \exp \left[-\frac{(\Delta x \cos \theta_{\text{turb}} + \Delta y \sin \theta_{\text{turb}})^2}{\ell_{\text{max}}^2} \right] \times \exp \left[-\frac{(\Delta x \sin \theta_{\text{turb}} - \Delta y \cos \theta_{\text{turb}})^2}{\ell_{\text{min}}^2} \right]. \quad (10)$$

The correlation function defines the shape of the average turbulent structure, which is elongated and tilted by an angle θ_{turb} with respect to the x -direction. Furthermore equation (10) shows that ℓ_{max} and ℓ_{min} are correlation lengths along the major and minor axes, respectively.

It is useful to write equation (10) as

$$C_{\Delta x}(\Delta y) = \exp \left[-\frac{(\Delta x)^2}{L_x^2} \right] \exp \left[-\frac{(\Delta y - \overbrace{m \Delta x}^{\Delta y_{\text{max}}})^2}{L_y^2} \right], \quad (11)$$

where

$$L_x = \ell_{\text{max}} \cos \theta_{\text{turb}} \left[1 + \frac{\ell_{\text{min}}^2}{\ell_{\text{max}}^2} \tan^2 \theta_{\text{turb}} \right]^{1/2}, \quad (12)$$

$$L_y = \frac{\ell_{\text{min}}}{\cos \theta_{\text{turb}}} \left[1 + \frac{\ell_{\text{min}}^2}{\ell_{\text{max}}^2} \tan^2 \theta_{\text{turb}} \right]^{1/2}, \quad (13)$$

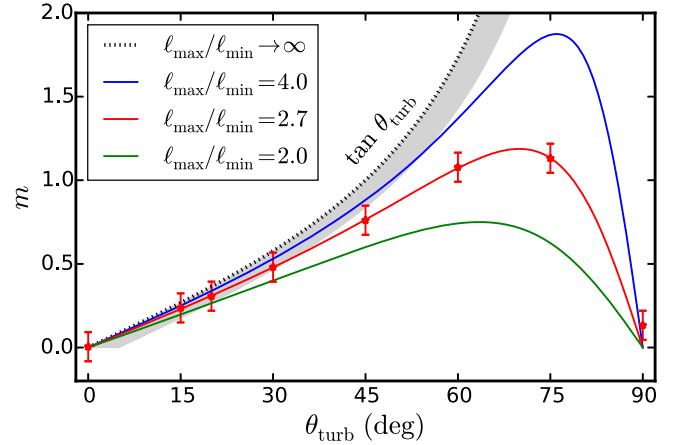


Figure 4. Slope m as a function of the tilt angle θ_{turb} for different turbulence elongation $\ell_{\text{max}}/\ell_{\text{min}}$ values. Data obtained from synthetic turbulence (red symbols) are in agreement with the results of equation (14).

$$m = \tan \theta_{\text{turb}} \left[\frac{1 - (\ell_{\text{min}}/\ell_{\text{max}})^2}{1 + (\ell_{\text{min}}/\ell_{\text{max}})^2 \tan^2 \theta_{\text{turb}}} \right]. \quad (14)$$

For each Δx , equation (11) gives a Gaussian peak with amplitude C_{max} , width L_y , and centred at $\Delta y_{\text{max}} = m \Delta x$, which is in agreement with the cross-correlation function depicted in figure 2(a). L_x and L_y are the correlation lengths in the x - and y -directions, respectively. The linear dependence with m predicted from equation (14) has been depicted by a solid line in figure 2(b). A good match to results of synthetic turbulence data (symbols) is obtained.

If L_x , L_y and m are known, the system of equations (12)–(14) can be inverted for obtaining the parameters characteristic of the turbulence: ℓ_{max} , ℓ_{min} , and θ_{turb} . Nevertheless accurate and simultaneous measurements of L_x , L_y and m are challenging and impractical in experiments. In the following, the use of m only for the determination of the tilt angle is assessed.

The slope m computed with equation (14) is shown in figure 4 for a scan of the tilt angle θ_{turb} and three values of elongation $\ell_{\text{max}}/\ell_{\text{min}}$. The red symbols are results of synthetic turbulence for the same elongation as in figures 1 and 2. The agreement between the analytical expression and the synthetic data confirms the dependence of m on the turbulence parameters given in equation (14). For all three cases and small θ_{turb} , m increases as the structure's major axis misaligns with respect to the x -axis, whereas for finite elongation and θ_{turb} close to 90° , m decreases as the structure's minor axis aligns with the x -axis. As a result of these behaviours, m has a maximum whose position depends on the elongation. For the three cases, it is in the range 65° – 75° .

Since m increases with the tilt angle in a broad θ_{turb} range, m can be used to estimate directly the tilt angle. The bracket term in equation (14) can be approximated by 1 in the limit of large elongation ($\ell_{\text{max}}/\ell_{\text{min}} \gg 1$) obtaining,

$$m \approx \tan \theta_{\text{turb}}. \quad (15)$$

This approximation is depicted in figure 4 by a dotted black line. For small θ_{turb} , it gives a reasonable approximation to the

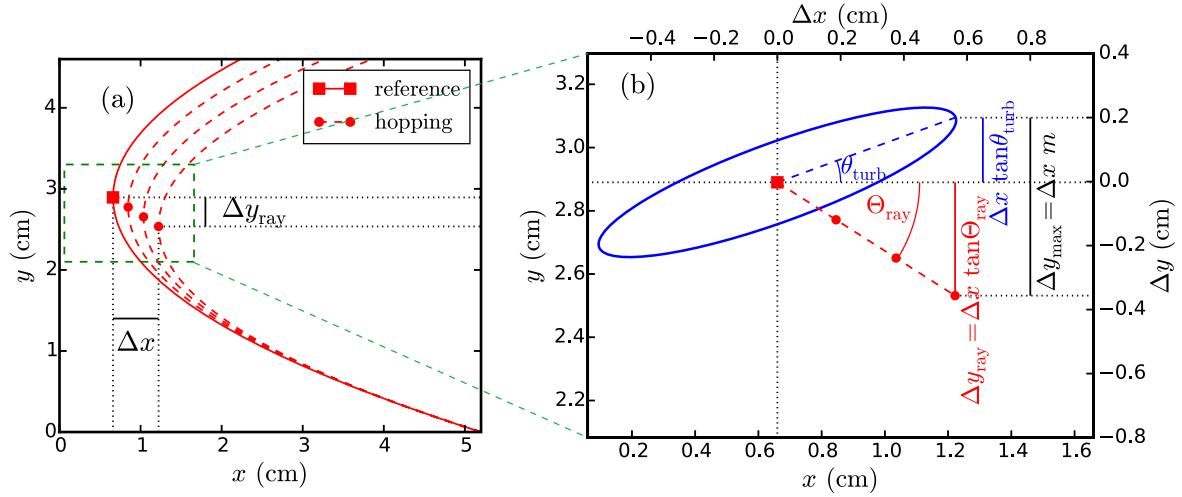


Figure 5. (a) Rays of the reference and three hopping Doppler reflectometry channels in slab geometry. The measurement positions are indicated with a square and circles. Δx and Δy_{ray} are depicted for one case. (b) Zoom showing schematically the effect of the vertical displacement of the measurement positions on the Δy_{max} measurement. Refer to the text for more details.

other curves, hence equation (15) can be used to obtain the tilt angle, however the accuracy and range of validity of this approximation depends on the elongation $\ell_{\text{max}}/\ell_{\text{min}}$. For a tolerance of 5° (grey shadowed area), in the $\ell_{\text{max}}/\ell_{\text{min}} = 2.7$ case it is valid up to 33° ; whereas for $\ell_{\text{max}}/\ell_{\text{min}} = 4.0$ the approximation is more accurate and the validity range increases to 54° . For larger θ_{turb} , $\tan \theta_{\text{turb}}$ is above the exact solution hence the tilt angle one would obtain with equation (15) is underestimated. For θ_{turb} close to 90° the approximation fails since arbitrarily large m are predicted, nevertheless this case corresponds to structures aligned along the flux surfaces which is unlikely [19]. It is concluded that equation (15) allows to obtain the tilt angle for reasonable elongation and tilting values.

2.4. Perpendicular displacement effect

Equations (7) and (8) assume that both Doppler channels are measuring at the same y -position. As a consequence, equation (15) considers contributions to the time delay coming only from the structure tilt. This is valid only for normal incidence where the measurement positions are radially aligned. However, due to the oblique angles of incidence used in Doppler reflectometry, the radial scan results also in a perpendicular displacement of the measurement position. This is shown in figure 5(a) where rays for different probing frequencies in slab geometry are depicted. The measurement positions of the reference and hopping channels are indicated with a square and circles, respectively. The change in the radial position Δx causes a perpendicular displacement Δy_{ray} of the measurement position.

For a small cutoff separation the measurement points are aligned along a straight line defining an angle Θ_{ray} with respect to the x -axis which fulfils

$$\Delta y_{\text{ray}} = \tan(\Theta_{\text{ray}}) \Delta x. \quad (16)$$

The geometrical definition of Θ_{ray} is shown in the zoom in figure 5(b). The upper and right axes indicate Δx and Δy , respectively.

The perpendicular displacement of the measurement points introduces an extra contribution to Δy_{max} and therefore to m . This extra contribution results from geometrical considerations as shown in figure 5(b). The measurement positions are depicted by red points and a schematic turbulent structure is shown with the blue contour. The measurement Δy_{max} (indicated with a black line) is the sum of contributions from the ray displacement $\Delta y_{\text{ray}} = \Delta x \tan \Theta_{\text{ray}}$ (red line) and the structure tilt $\Delta x \tan \theta_{\text{turb}}$ (blue line). Therefore

$$m = \tan \theta_{\text{turb}} - \tan \Theta_{\text{ray}}. \quad (17)$$

Concluding, it is important to consider the perpendicular displacement of the measurement positions, which has an impact on Δy_{max} (hence on the time delay τ_{max}) and m . Equation (17) is the basis of the measurement method of the tilt angle. For specific applications, the signs of the different terms have to be adjusted to the sign convention of time delay, angle and velocity. In section 4.2, this equation will be used for analysing the experimental data and for obtaining the tilt angle.

2.5. Discussion of diagnostic effects

The method previously presented assumes point like and linear measurements of density fluctuations (see equation (6)). This supposes a large simplification of the diagnostic response of a Doppler reflectometer which is known to be complex [29, 37, 41, 42]. Here, the implications and validity of such an approximation are discussed, as well as possible limitations to the applicability of the method.

Contributions to the Doppler reflectometer signal come from a rather extended scattering region close to the cutoff, where the electric field of the probing wave is maximum. The size of such a region along the radial direction defines

the radial resolution of the diagnostic which is typically in the mm range. Along the perpendicular direction, the size of the scattering region is approximated by the beam width w at the cutoff, which is typically of the order of few cm and is an important parameter defining the spectral resolution of the diagnostic [29]. In the appendix, an extended scattering region and the k_{\perp} selectivity have been considered for the calculation of the cross-correlation function. It is concluded that the time delay and slope m remain unaffected if the radial correlation length L_x is larger than the radial resolution δr . Moreover, it has been verified in the appendix that for Gaussian wavenumber spectra the k_{\perp} selectivity has no impact on the correlation analysis. Nevertheless, deviations from Gaussian [9, 45] may induce a dependence of the mentioned quantities with k_{\perp} . Furthermore, micro-instabilities at different scales (k_{\perp}) may drive turbulence with different characteristics. In this paper, turbulence characteristics as the tilt angle are regarded as averaged on the experimentally measured k_{\perp} range. The study of more general spectral shapes as well as k_{\perp} dependence of the correlation measurements are left for future work.

Although the backscattering at the cutoff provides the strongest component of the Doppler reflectometry signal, scattering along the beam path also contributes. Albeit small in amplitude, this component often called *forward* or *small angle scattering* in literature, may have an important impact on the correlation analysis [36, 41]. Forward scattering may provide significant correlation values at large radial separations for which no correlation is expected from the cutoff contributions. This effect produces a slow decay of the correlation function predicted in theory [41] and observed in simulations [42]. The impact of forward scattering can be minimized by restricting the analysis to small radial separations with high correlation levels only, for which the backscattering at the cutoff is the dominant contribution to the cross-correlation function. In this paper, cases with correlation level above 0.6 are only considered.

Another contribution to the Doppler reflectometer signal is provided by the *direct reflection* which may be collected by the antenna. This component often called *zero-order*, is not Doppler shifted [29, 46]. This contribution may corrupt the correlation analysis and hence the measurement of the tilt angle. Nevertheless, it can be excluded from the analysis by filtering out small frequency components of the Doppler signal.

Finally, the method assumes the reflectometer signal proportional to the density fluctuations. This corresponds to the *linear regime* in which the reflectometers signal is built by single scattering contributions [37]. The linear regime is expected for small turbulence level, e.g. in the core of fusion plasmas. Nevertheless, for increasing turbulence level, a transition into the *nonlinear regime* is expected, e.g. in the scrape-off layer. The transition into nonlinear regime has been widely investigated in literature [9, 36, 37, 39, 42]. Moreover, it has been shown that the nonlinear regime is produced by multiple scattering events from different wavenumbers [37], which are poorly correlated and may degrade the cross-correlation function. Accordingly, full-wave simulations have obtained a reduced correlation level in the nonlinear regime [42]. Therefore the applicability of the method in the

nonlinear regime seems unrealistic, though this is still to be confirmed by detailed nonlinear studies in the future, e.g. using full-wave simulations.

3. Temporal decorrelation of the turbulence

Until now, frozen turbulence has been assumed in the tilt angle measurement method. This is a valid assumption if the turbulent structures do not change appreciably while they propagate through the scattering region where the Doppler reflectometry measurements are performed. This condition may not be fulfilled in general due to the self-dynamics of the turbulence responsible for creation, mutation and destruction of structures in the plasma frame. The time scale characteristic for these processes is given by the turbulence decorrelation time τ_d . It is of the order of few μs in fusion plasmas and can be interpreted as the mean life time of turbulent structures. In this section, the effect of the turbulence decorrelation is considered including a Gaussian correlation function in time [47], and a correction factor applicable to the characterization method accounting for such effect is derived. At the end, a more realistic correlation function is discussed [48].

The cross-correlation function for a given radial separation Δx and considering the decorrelation time of the turbulence is

$$C_{\Delta x}(\tau) = C_{\max} \exp\left[-\frac{(u_{\perp}\tau - \Delta y_{\max})^2}{w^2}\right] \exp\left(-\frac{\tau^2}{\tau_d^2}\right), \quad (18)$$

where the time lag τ has been explicitly used. The first two terms correspond to the correlation function for the frozen turbulence case as in equation (11), where C_{\max} and Δy_{\max} are defined by the 2D structure of the turbulence (equations (12) and (14)). The beam width w has been used instead of L_y because, different to the point like measurement, the extension of the scattering region defines to a large extent the width of the cross-correlation function (see appendix). The last term in equation (18) includes a Gaussian correlation function in time [47].

The correlation function $C_{\Delta x}(\tau)$ is plotted in figure 6 for $w = 4.0$ cm, $u_{\perp} = 1$ km s⁻¹ and $\Delta y_{\max} = 1.0$ cm. Colours indicate different τ_d values. The blue line for $\tau_d \rightarrow \infty$ shows a peak centred at $\tau_{\max} = \Delta y_{\max}/u_{\perp} = 10$ μs as in the frozen turbulence case. As τ_d decreases the peak becomes narrower and moves closer to $\tau = 0$, implying a reduction of the measured time delay τ_{\max} . This effect is small for $\tau_d = 119$ μs (green line) with a time delay 10% shorter than the one of the frozen case, whereas it is strong for $\tau_d = 13$ μs (light blue line) with a time delay reduced by 90%.

It can be shown that $C_{\Delta x}(\tau)$ from equation (18) is maximal at the time delay given by

$$\tau_{\max} = \frac{\Delta y_{\max}}{u_{\perp}} \left(1 + \frac{w^2}{u_{\perp}^2 \tau_d^2}\right)^{-1} = \frac{\Delta y_{\max}}{u_{\perp}} F_d. \quad (19)$$

The first term gives the time delay expected from the frozen turbulence case, and the second term is a correction factor F_d related to the temporal decorrelation that reduces the

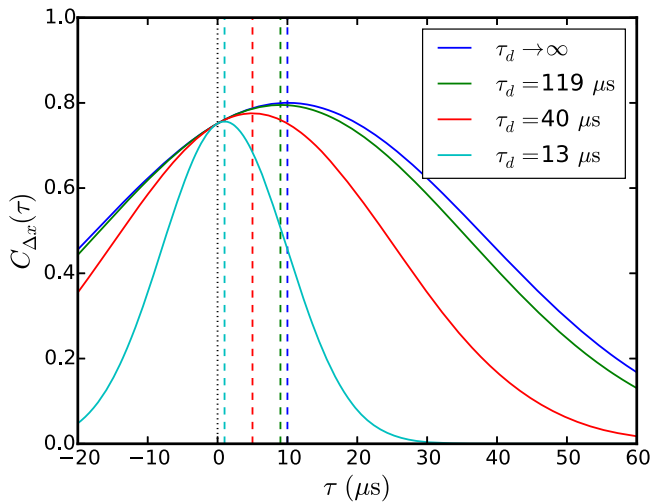


Figure 6. Cross-correlation function from equation (18) for different τ_d values. The blue curve corresponds to the frozen turbulence case.

measured time delay. It is relevant for $\tau_d \leq w/u_\perp$, that is if the life time of the structure is smaller or comparable to its passing time in front of the beam w/u_\perp .

The time delay reduction leads to an underestimation of m . This effect can be included in equation (17) with the correction factor F_d as follows:

$$m = F_d [\tan(\theta_{\text{turb}}) - \tan(\Theta_{\text{ray}})]. \quad (20)$$

The impact of the decorrelation time in the experiments can be assessed by comparing the passing time w/u_\perp with τ_d measurements or estimates [47, 49]. For large plasma flow velocities the passing time is substantially smaller than τ_d and the temporal decorrelation has no impact, whereas for small velocities the passing time is comparable to or larger than τ_d and the correction factor F_d is needed in the analysis. Equation (20) will be used in sections 4.3 and 5 for obtaining the tilt angle.

Equation (19) relates the correction factor F_d with τ_d and other experimental parameters. Nevertheless this numerical relationship relies on several approximations i.a. Gaussian correlation function in both space and time. The correlation function of real turbulence may deviate from Gaussian and resemble a Lorentzian function [48, 50]. The analysis presented in this section has been repeated for a Lorentzian correlation function in time. Although the results are qualitatively equivalent, a smaller F_d has been obtained compared with the Gaussian case; for $\tau_d = 13 \mu s$ 50% difference has been observed. Summarizing, equation (19) is accurate only for the considered model and should be regarded only as a rough estimate when applied to the analysis of experimental data.

4. Measurements on the ASDEX Upgrade tokamak

In this section, the tilt angle measurement method is applied on the ASDEX Upgrade tokamak (AUG), which has major and minor radii of 1.65 and 0.5 m. Two L-mode discharges in the lower single null magnetic configuration, with 0.8 MA plasma current and 2.5 T on-axis magnetic field are analysed.

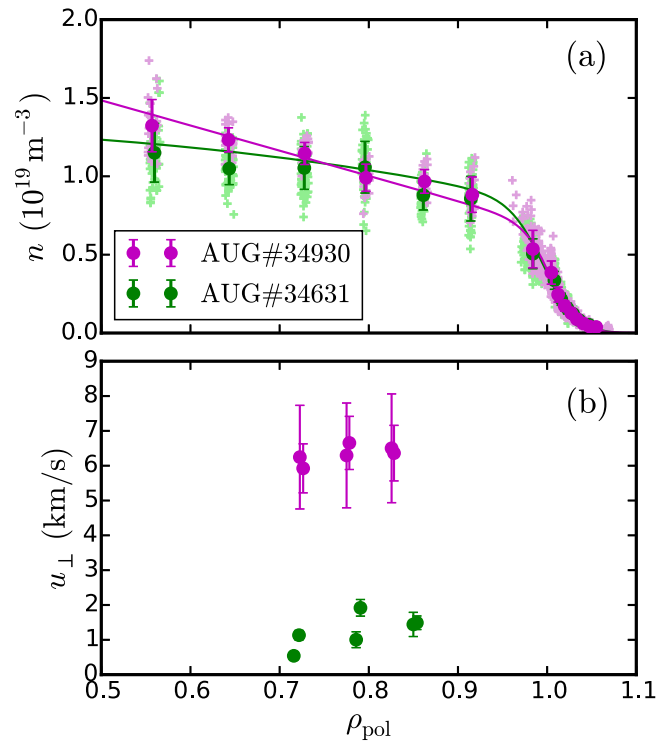


Figure 7. Radial profiles of (a) plasma density and (b) perpendicular flow velocity for AUG discharges #34930 with ECRH and NBI, and #34631 with only ECRH. The solid lines in (a) are the fits used as input for the ray tracing.

In the AUG discharge #34930, auxiliary heating has been provided by electron cyclotron resonance heating (ECRH, 1.5 MW) and neutral beam injection (NBI, 0.8 MW). In the discharge #34631 only 1.5 MW of ECRH are applied. The NBI is used in order to induce toroidal plasma rotation which results in a higher u_\perp than in the ECRH only case. This allows to apply the tilt angle measurement method on discharge #34930 avoiding corrections due to the decorrelation time of the turbulence. Discharge #34631 without NBI has low u_\perp and is used to investigate the effect of the temporal decorrelation of the turbulence on the measurements (see section 3) at the end of this section.

The plasma density profiles for both discharges are shown in figure 7(a). ρ_{pol} is the normalized poloidal flux radius, which is 0 at the magnetic axis and 1 at the last closed flux surface. The measurements depicted with symbols are obtained from Thomson scattering [51] and lithium beam diagnostics [52]. The solid lines depict the fits which are used for ray tracing calculations with the TORBEAM code [53].

4.1. Experimental setup

Doppler reflectometry measurements have been performed with the steerable mirror system installed in AUG [9, 54], which allows to modify the angle of incidence of the probing beam in the plasma during the discharge. Two V-band reflectometry channels (50–75 GHz) probing in extraordinary (X) mode polarization have been used. The reflectometers have been developed by LPP and are similar to the systems described in [55]. The reference channel probes three

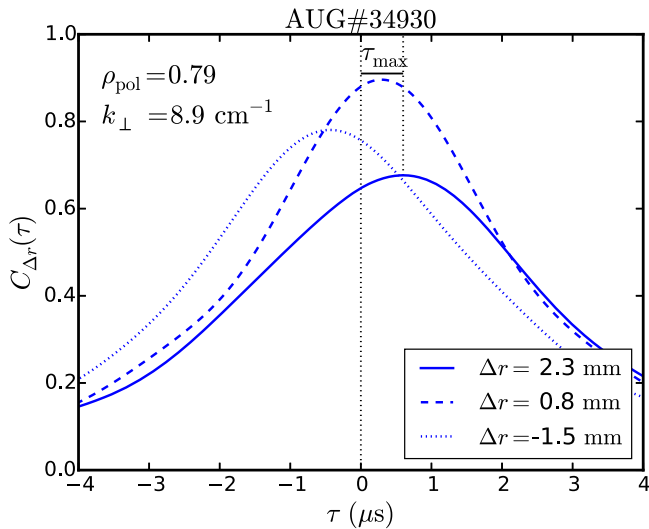


Figure 8. Cross-correlation function of the reflectometer signals from AUG. The reference channel probes at $\rho_{pol} = 0.79$ and $k_{\perp} = 8.9 \text{ cm}^{-1}$. Three radial separations Δr are included. The time delay τ_{max} is indicated for one case.

frequencies (50 ms each), and the hopping channel probes 10 frequencies around the reference one with 5 ms per frequency. The same frequency pattern is used for four angles of incidence of the probing beam. The probed radial range is $\rho_{pol} = 0.70\text{--}0.84$, and the perpendicular wavenumber is in the range $k_{\perp} = 3.0\text{--}9.0 \text{ cm}^{-1}$. It corresponds to $k_{\perp} \rho_s = 1.1\text{--}3.4$ where $\rho_s = \sqrt{2m_i T_e} / (eB)$ is the ion Larmor radius evaluated at electron temperature.

The u_{\perp} profile has been computed from the Doppler reflectometry data. The results for both discharges are shown in figure 7(b). For discharge #34930 an approximately constant velocity of $u_{\perp} \approx 6 \text{ km s}^{-1}$ is obtained. Discharge #34631 has $u_{\perp} \approx 1 \text{ km s}^{-1}$, which is considerably lower because of the absence of torque input by NBI.

4.2. Tilt angle measurement

The time delay of the cross-correlation function is first investigated experimentally for the AUG discharge #34930. The results are analysed based on the modelling presented in section 2, allowing for the measurement of the tilt angle of turbulent structures in the confined region of AUG.

The cross-correlation function of the reflectometer signals $C_{\Delta r}(\tau)$ has been computed using equation (2). Three examples are shown in figure 8. The reference channel probes at $\rho_{pol} = 0.79$ and $k_{\perp} = 8.9 \text{ cm}^{-1}$. The hopping channel probes two outer-more positions with positive radial separations Δr and one inner-more with negative Δr . In all cases, a peak displaced from $\tau = 0$ is obtained similarly to the synthetic data in figure 2(a). The position of the maximum gives the time delay τ_{max} as indicated for the solid curve.

In the following, measurements around $\rho_{pol} \approx 0.8$ and three angles of incidence are considered. The measurement positions obtained with TORBEAM are shown on the poloidal cross-section of AUG in figure 9(a). Closed and open flux surfaces are depicted by solid and dashed grey lines,

respectively. The magnetic axis is indicated with a ‘x’ and wall elements are plotted. Figure 9(b) shows the zoom to the region of interest. The three sets of points in different colours correspond to three angles of incidence. The measurement positions are depicted with squares and circles for reference and hopping channels, respectively. The insets show the geometry of the measurement positions in detail. One turbulent structure is schematically depicted.

Due to the different angle of incidence of the probing beam, the point sets in figure 9(b) have a different alignment with respect to the radial direction indicated with a dashed grey line. The blue points are strongly misaligned with respect to the radial direction defining an angle of $\Theta_{ray} = -40.9^\circ$, whereas green points are slightly better aligned with $\Theta_{ray} = -24.9^\circ$. The red points are almost aligned with respect to the radial direction with $\Theta_{ray} = 5.7^\circ$. Note that the sign is opposite compared to the previous two cases.

The time delay τ_{max} at the maximum of the cross-correlation function has been computed and multiplied by u_{\perp} in order to obtain the perpendicular displacement $\Delta y_{max} = u_{\perp} \tau_{max}$. The results of $u_{\perp} \tau_{max}$ as function of Δr are shown in figure 9(c) for the three measurement positions depicted in figure 9(b) by the same colours. A linear dependence is observed. Linear functions are fitted to the data and are depicted by dashed lines in figure 9(c). The fits have a different slope m for the three cases shown. The empty blue symbols correspond to the cases depicted in figure 8.

The tilt and propagation direction of the structure depicted in figure 9(b) are consistent with the time delays presented in figure 9(c). The structure is strongly misaligned with respect to the blue measurement positions, hence it is ‘seen’ first by the inner-more measurement positions and later by the reference channel as it propagates downwards, thus a negative time delay is obtained for $\Delta r < 0$. Additionally, the structure is ‘seen’ first by reference and later by the outer-more positions obtaining a positive time delay for $\Delta r > 0$. Contrarily, the structure is almost aligned with the red measurement positions, therefore shorter time delays are obtained. The unique tilt angle valid for all three positions and indicated in the figure is calculated next.

The slope m obtained from all the measurements in the range $\rho = 0.70\text{--}0.84$ is plotted as a function of Θ_{ray} in figure 9(d). The blue, green and red data points correspond to the cases shown in figure 9(c). The data show a clear trend of m with Θ_{ray} . The prediction of equation (17) for non-tilted structures ($\theta_{turb} = 0$) is depicted in figure 9(d) by a dashed black line. The experimental data show a similar behaviour but are vertically shifted due to the tilt of the turbulent structures. If a constant tilt is assumed in the measurement region, the data in figure 9(d) can be fitted with equation (17) with the tilt angle θ_{turb} as the only free parameter. The fit is depicted by the magenta solid line in the figure. The good quality of the fit shows that the time delays are explained by a single average tilt angle of the turbulent structures as discussed in section 2. The tilt angle is

$$\theta_{turb} = (18 \pm 7)^\circ, \quad (21)$$

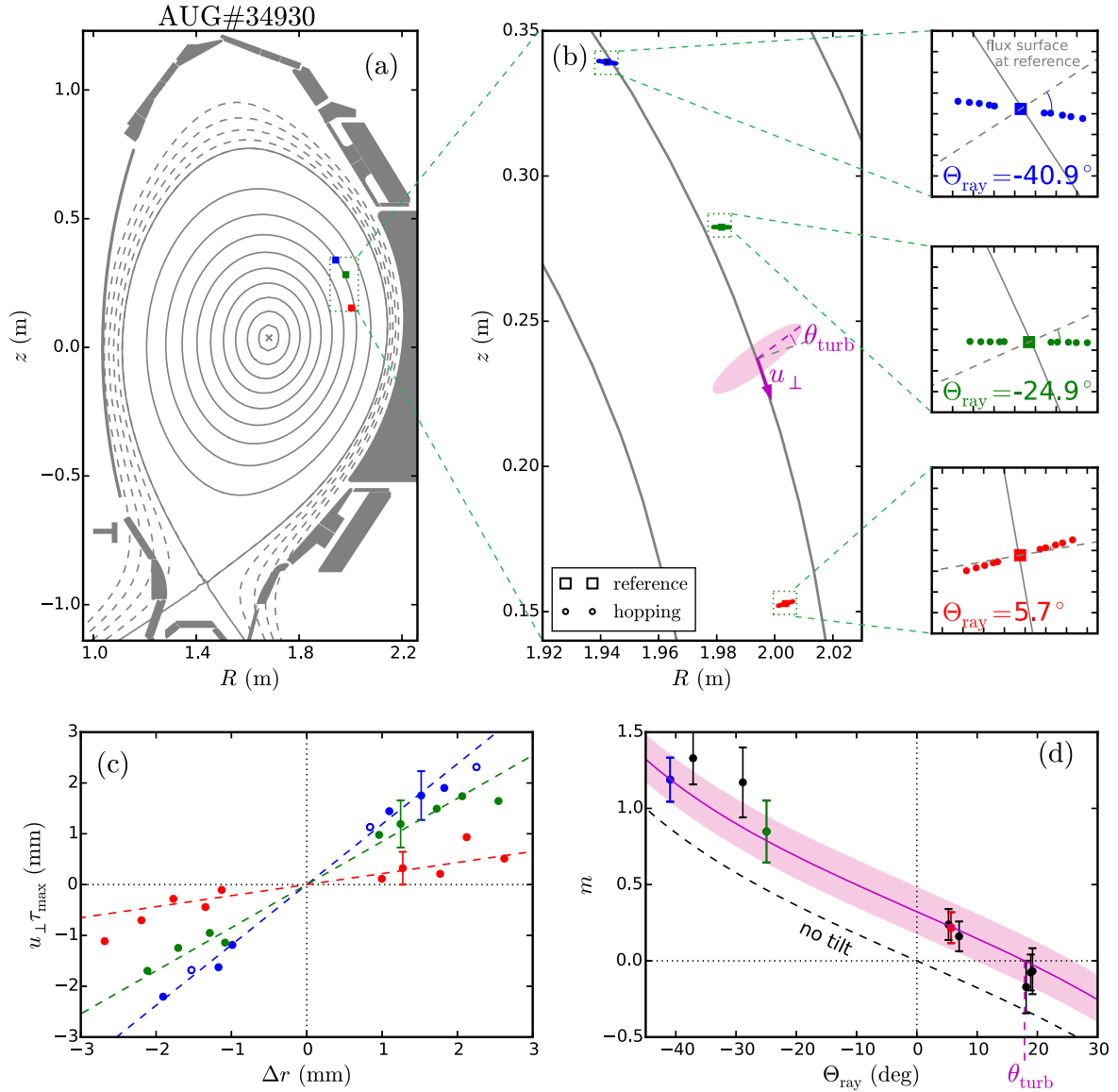


Figure 9. (a) Doppler reflectometry measurement positions on the AUG cross-section and (b) zoom to the region of interest. One turbulent structure is schematically depicted, the tilt angle and propagation velocity are indicated. (c) Perpendicular displacement $\Delta y_{\text{max}} = u_{\perp} \tau_{\text{max}}$ computed from the time delay of the cross-correlation function versus the radial separation Δr . The dashed lines depict linear fits to the data. (d) Slope m as a function of Θ_{ray} . The fit to the data with equation (17) is depicted by a magenta line. Refer to the text for more details.

as indicated in the plot at the intersection with the $m = 0$ axis, at which the structure is aligned with the measurement points. The error bar is illustrated as a shadowed area around the fit. A structure with the corresponding tilt is schematically depicted in figure 9(b).

Given the large value of u_{\perp} , no correction factor ($F_d = 1$) accounting for the decorrelation time effect is required (see section 3). The passing time of the structures is about $w/u_{\perp} \approx 3 \mu\text{s}$, which is smaller than the decorrelation time $\tau_d \approx 9 \mu\text{s}$ measured with poloidal correlation reflectometry (PCR). This is a diagnostic recently installed on AUG used for turbulence investigation at scale $k_{\perp} \approx 1 \text{ cm}^{-1}$ [47, 49]. Furthermore, fitting the data of figure 9(d) using equation (20) with F_d as a free parameter gives a value of 1.1 ± 0.2 . This is in agreement with the frozen turbulence approximation which is suitable for this case.

It has been mentioned in section 2.2, that a radial propagation of turbulent structures may produce extra contributions to the time delay so far not considered. In discharge #34930, a radial velocity of up to 6 km s^{-1} would be necessary in order to explain the measured time delays (see figure 9(c)). Such a large radial velocity is unrealistic in the confined region of fusion plasmas [29, 43, 44], thus radial propagation might lead to minor corrections only. Furthermore, one can estimate that radial velocities up to $\tan(\Delta\theta_{\text{turb}})u_{\perp}$ can be tolerated for obtaining θ_{turb} values within the experimental error bars $\Delta\theta_{\text{turb}}$. In this case, the tolerance is $0.12 u_{\perp}$ (see equation (21)).

The previous measurements correspond to the ‘ECRH phase’ investigated in [28], where the experimental data was compared with results from the linear ballooning theory. This

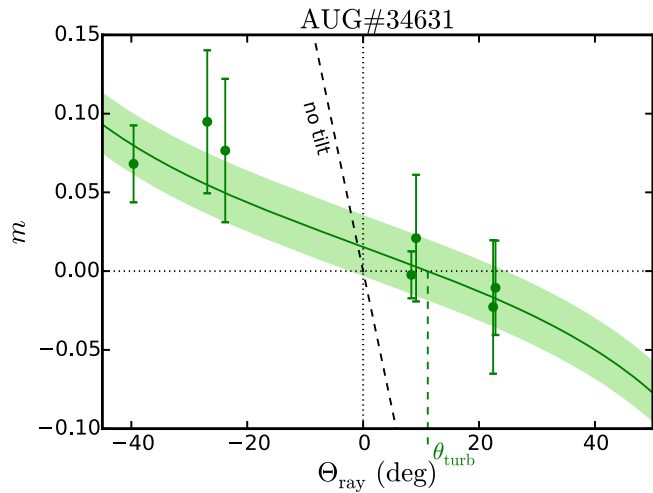


Figure 10. Slope m as a function of Θ_{ray} for AUG discharge #34631. The solid line depicts the fit to the data using equation (20).

simple model estimates the tilt angle as [17, 19]

$$\theta_{\text{turb}} \approx -\text{sign}[\hat{s}(\partial_r v_{\text{ph}} + \partial_r u_{E \times B})] \times \left| \frac{\partial_r v_{\text{ph}} + \partial_r u_{E \times B}}{2\gamma\hat{s}} \right|^{1/3}, \quad (22)$$

where γ is the growth rate of the unstable mode, \hat{s} is the magnetic shear and ∂_r denotes the radial derivative. Equation (22) includes two effects on the tilt angle, namely the sheared $E \times B$ flow through $\partial_r u_{E \times B}$, and the the global structure of the unstable mode through the phase velocity shear $\partial_r v_{\text{ph}}$. An $E \times B$ shear of 16 kHz was obtained from CXRS measurements [56], and a phase velocity shear of 6 kHz was computed from linear simulations with the gyrokinetic code GKW [57]. Such simulations showed also that turbulence was dominated by trapped electron modes locally destabilized by electron temperature gradient with a normalized scale length of 9. The tilt angle estimated with equation (22) was 21° , which is within the experimental error bars (see equation (21)). The large $\partial_r u_{E \times B}$ value, and the similarity of measured and estimated tilt angles, demonstrated the dominant effect of the $E \times B$ shear on turbulent structures in the plasma core [28].

4.3. Small propagation velocity and τ_d correction

The AUG discharge #34631 is used to investigate the impact of the temporal decorrelation of the turbulence on the tilt angle measurements for the same reflectometer configuration as for #34930. According to section 3, a strong impact on the time delays is expected because of the small plasma velocity u_\perp (see figure 7(b)). The passing time for this case, $w/u_\perp \approx 20 \mu\text{s}$, is longer than the decorrelation time of $\tau_d \approx 14 \mu\text{s}$ obtained with the PCR system, therefore a strong effect of the temporal decorrelation of the turbulence is expected.

The measured time delays and consequently the slope m are small for #34631. The slope for the measurements in the range $\rho_{\text{pol}} = 0.70\text{--}0.84$ is shown in figure 10. The values are

considerably smaller than the prediction of equation (17) for non-tilted structures and frozen turbulence (dashed black line), and also smaller than those for discharge #34930 (see figure 9(d)). It is concluded that the data cannot be described by equation (17) which is valid for frozen turbulence, instead they are described by equation (20) which accounts for the temporal decorrelation through the factor F_d . The fit using equation (20) with θ_{turb} and F_d as free parameters is shown in figure 10 with a solid line. The tilt angle and correction factor are

$$\theta_{\text{turb}} = (11 \pm 13)^\circ, \quad (23)$$

$$F_d = (7 \pm 2) \times 10^{-2}. \quad (24)$$

The large error bars of the tilt angle are due to the large error bars of the single m values and the scatter of the data. Although in this case the tilt angle is not determined with a good accuracy, the anisotropy of the turbulence is indicated.

5. Measurements on the TJ-II stellarator

In this section the tilt angle measurement method is applied on TJ-II, a heliac type stellarator with major and minor radii of 1.5 and 0.2 m. One series of reproducible discharges is investigated (#43459-91). The scenario is a low density (line averaged density $5.5 \times 10^{19} \text{ m}^{-3}$) L-mode discharge in the standard magnetic configuration with 1 T on-axis. An ECRH power of 0.5 MW is applied. Similar discharges have been recently investigated using the gyrokinetic code EUTERPE [58]. It was found that turbulence is dominated by trapped electron modes locally destabilized by electron temperature gradient with a normalized scale length of 30.

The density profile is shown in figure 11(a). It has been obtained by Bayesian inference of Thomson scattering, interferometry and reflectometry data [59]. ρ is the normalized effective radius. This profile is used as input for ray tracing calculations with the TRUBA code [60].

5.1. Experimental setup

Doppler reflectometry measurements have been performed using the system installed in TJ-II [31], which allows to modify the angle of incidence of the microwave beam in the plasma on a shot-to-shot basis. Two Q-band (33–50 GHz) channels probing in the X-mode polarization have been used. For the detailed correlation measurements presented next, the reference channel probes at fixed frequency during the discharge, while the hopping channel probes at 12 frequencies (5 ms each) around the reference one. A broad scan of the angle of incidence has been performed. The probing frequencies have been specifically chosen to probe at a radial position of $\rho = 0.72$. The probed wavenumbers are in the range $k_\perp = 2.0\text{--}9.0 \text{ cm}^{-1}$ corresponding to $k_\perp \rho_s = 0.5\text{--}2.5$.

Additionally, a fine scan of the probing frequency in the range 33–39 GHz has been performed with both channels. This scan allows to compute the u_\perp profile depicted in figure 11(b). This diagnostic configuration will be further

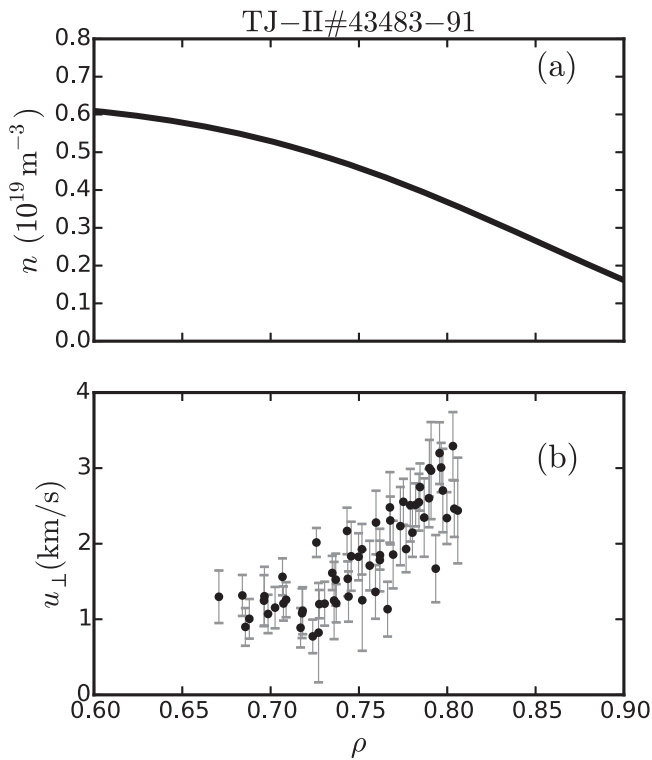


Figure 11. Radial profiles of (a) plasma density and (b) perpendicular velocity u_{\perp} for the TJ-II discharges.

discussed in section 5.3 where a two-point correlation technique is presented.

5.2. Tilt angle measurement

The time delay of the cross-correlation function is investigated for the measurements at $\rho = 0.72$. Experimental data are analysed in a similar way as for AUG in section 4.2. Measurements of the tilt angle of the turbulent structures in the confined region of TJ-II are obtained for the first time.

The measurement positions obtained with TRUBA are shown on the perpendicular cross-section of TJ-II in figure 12(a). Closed flux surfaces are depicted by solid grey lines, the magnetic axis is indicated with an ‘x’, and a section of the vessel is shown. Figure 12(b) shows in detail the measurement positions of reference (squares) and hopping (circles) channels. The eight sets of points correspond to different angles of incidence of the probing beam. Measurements are differently aligned; the blue measurement points define a negative (clockwise) angle Θ_{ray} with respect to the radial direction, while the red ones define a positive one (counter-clockwise). The scan of the angle of incidence provides a broad Θ_{ray} scan between -60° and $+40^{\circ}$. Turbulent structures are artistically depicted.

The cross-correlation function has been computed and the time delays τ_{max} have been obtained as discussed for AUG in section 4.2. Figure 12(c) shows the results of $u_{\perp} \tau_{\text{max}}$ as a function of Δr . Only points obtained with high correlation and hence a well defined time delay are considered. The colours correspond to the three coloured angles of incidence in figure 12(b). Linear fits to the data (dashed lines) show

different slopes m for the three cases, indeed a sign inversion between red and blue data is observed.

The structures tilt angle and propagation direction depicted in figure 12(b) are qualitatively consistent with the time delays of figure 12(c). Turbulent structures aligned with the green measurement points provide a small time delay. Moreover, due to the misalignment of the structures with respect to the blue (red) measurement points, the structures are ‘seen’ first (later) by the hopping channel for positive Δr , resulting in a negative (positive) time delay.

The slope m is plotted as a function of Θ_{ray} in figure 12(d) with blue, green and red data points corresponding to the cases presented in figure 12(c). A clear dependence of m on Θ_{ray} is observed. The prediction of equation (17) for $\theta_{\text{turb}} = 0$ is depicted in figure 12(d) by a dashed black line, which shows that m is substantially smaller than frozen turbulence expectations. The smallness of m would require the unlikely alignment of the turbulent structures with the measurement positions for all cases depicted in figure 12(b), if frozen turbulence is assumed. Moreover, the passing time of the structures in front of the beam is estimated as $w/u_{\perp} \approx 13 \mu\text{s}$, which is comparable to typical values for the decorrelation time of the turbulence τ_d [47]. The last two observations indicate that the frozen turbulence approximation is not valid for the present case.

The data of figure 12(d) have been fitted using equation (20) assuming a constant tilt angle θ_{turb} , F_d and θ_{turb} are free parameters obtained from the fit. The purple solid line in figure 12(d) depicts the fit obtained. It is remarkable that the fit recovers accurately the Θ_{ray} dependence of m for all measured angles. The good agreement between the experimental data and the fit shows that, although the decorrelation time of the turbulence has a strong impact on the time delays, equation (20) reproduces the experimental data and allows to compute the tilt angle of the turbulent structures. The tilt angle and factor are,

$$\theta_{\text{turb}} = (-29 \pm 9)^{\circ}, \quad (25)$$

$$F_d = (9.9 \pm 0.9) \times 10^{-2}. \quad (26)$$

The tilt angle is indicated in figure 12(d) as the interception with the $m = 0$ axis, and is used to draw the schematic structures in figure 12(b).

In the following, equation (19) is used to obtain τ_d from the experimentally measured correction factor F_d . Although this is regarded a rough estimate, it is the first experimental estimation of its kind done in TJ-II. Using equation (19), the decorrelation time of the turbulence can be estimated from F_d (equation (26)), $w = 2.0 \text{ cm}$ and $u_{\perp} = 1.5 \text{ km s}^{-1}$ to

$$\tau_d = \frac{w}{u_{\perp}} (F_d^{-1} - 1)^{-1/2} \approx 4 \mu\text{s}. \quad (27)$$

Further investigations regarding the accuracy of equation (19) as well as comparisons of this value with simulations and other experimental measurements are left for future work.

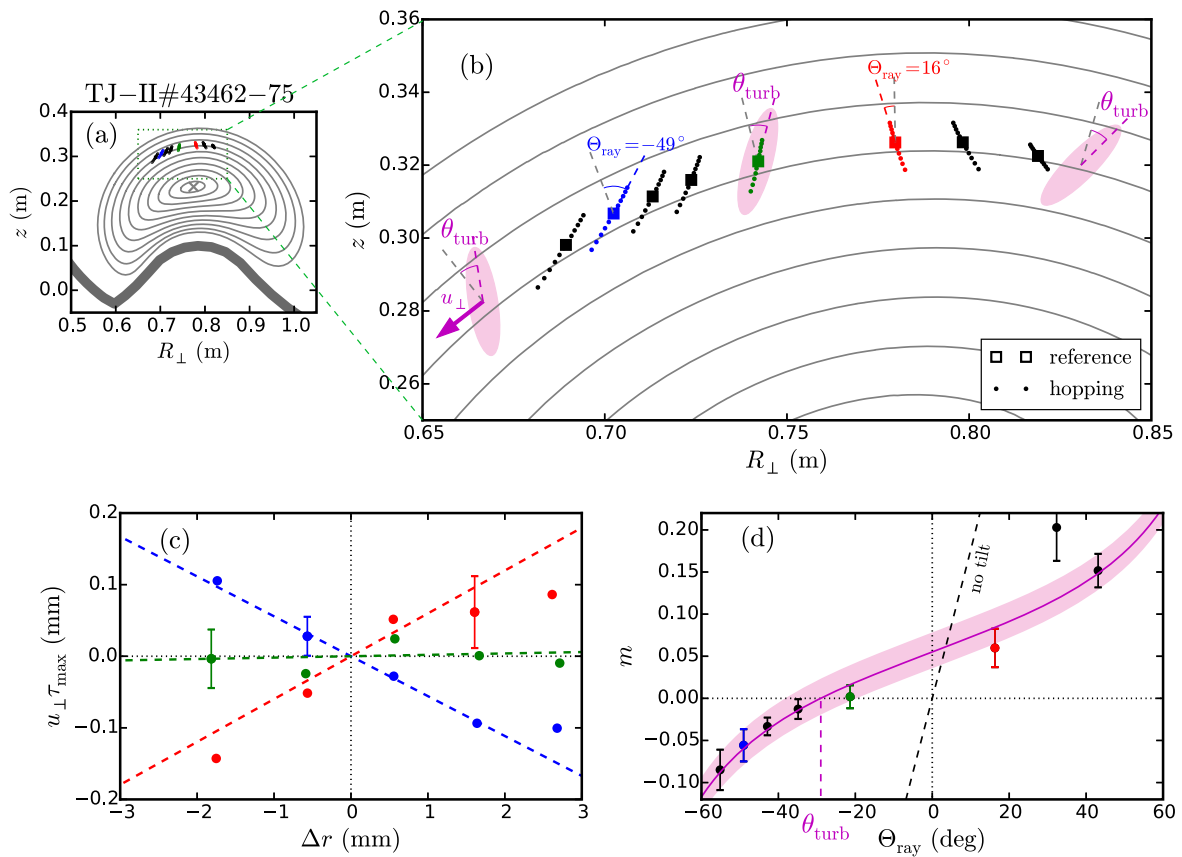


Figure 12. (a) Doppler reflectometry measurement positions on the perpendicular cross-section of TJ-II and (b) zoom to the region of interest. Turbulent structures are schematically depicted, the tilt angle and propagation velocity are indicated. (c) Perpendicular displacement $\Delta y_{\max} = u_{\perp} \tau_{\max}$ as a function of Δr . Results for three angles of incidence are presented (see colours in a and b). Linear fits are indicated with dashed lines. (d) Slope m as a function of Θ_{ray} . The fit of the data with equation (20) is depicted by the magenta line. Refer to the text for more details.

5.3. Radial profile of tilt angle

The radial profile of the tilt angle has been investigated by two-point correlation measurements. A fine scan of the probing frequency of both channels in the range 33–39 GHz has been performed. The frequency difference between the channels is fixed at 500 MHz, thus the cross-correlation function is obtained for only one Δr value per probed radial position. Four angles of incidence, two with $\Theta_{\text{ray}} < 0$ and two with $\Theta_{\text{ray}} > 0$, have been used. This configuration provides measurements at $k_{\perp} = 3.5$ or 5.5 cm^{-1} , which do not change appreciably within the radial scan.

The time delay τ_{\max} profiles for different angles of incidence (blue data with $\Theta_{\text{ray}} < 0$ and red with $\Theta_{\text{ray}} > 0$) are shown in figure 13(b). Note that the data sets have an opposite sign due to the opposite sign of Θ_{ray} leading to a different alignment of measurement positions with the turbulent structures. For the outermost positions around $\rho = 0.8$, the magnitude of τ_{\max} is larger for the blue than for the red data. This indicates a better alignment of the turbulent structure with the measurement positions with $\Theta_{\text{ray}} > 0$, obtaining a positive tilt angle. In contrast, for the inner positions around $\rho = 0.72$, τ_{\max} is larger for the red data indicating a better alignment with $\Theta_{\text{ray}} < 0$ measurement positions and hence negative tilt angle.

The slope is computed as $m = \tau_{\max} u_{\perp} / \Delta r$ for each radial position and angle of incidence. The tilt angle θ_{turb} and correction factor F_d are obtained by fitting the data in radial windows of size $\Delta \rho = 0.003$ with equation (20). The results are shown in figures 13(c) and (d), respectively. As expected from the time delay comparison, there is a change of the tilt angle from approximately -30° to $+20^{\circ}$ from the innermost to the outermost measurement positions. F_d increases towards the plasma edge. The u_{\perp} profile is shown in figure 13(a) for comparison.

At $\rho = 0.72$, the tilt angle and the correction factor agree with the values obtained in the previous detailed measurements (see equations (25) and (26)), which underlines the fact that a two-point correlation scan can provide radially resolved information on θ_{turb} and F_d . The increase of F_d is consistent with the u_{\perp} increase towards the plasma edge observed in figure 13(a). A faster structure propagation means that the decorrelation time of the turbulence has a smaller impact on the time delays, thus the correction factor approaches one (see equation (19)).

In the following some effects which may potentially be related with the radial change of tilt angle are discussed. The effect of u_{\perp} shear may play an important role [17–19]. In figure 13(a), a 3rd-order polynomial fit to u_{\perp} data is shown with a solid line, and its radial derivative with a dashed one.

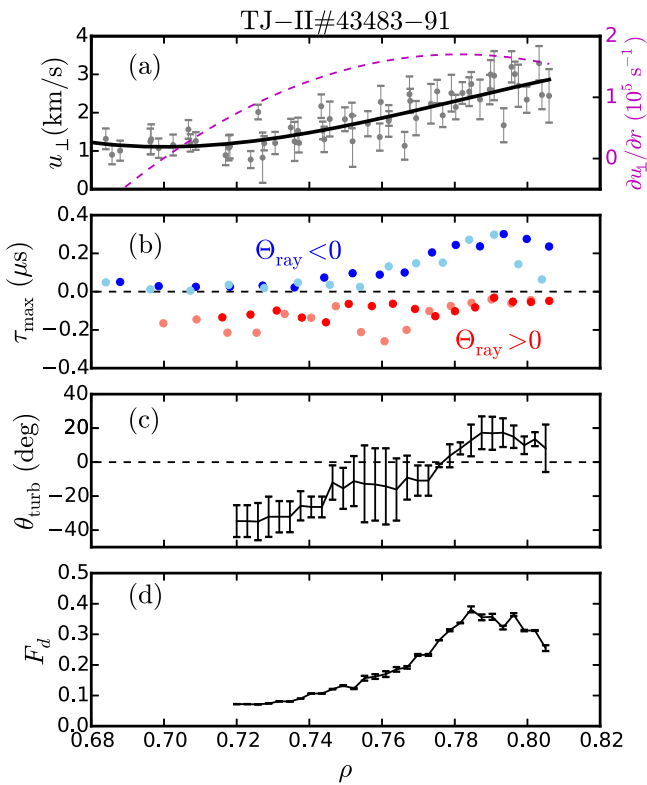


Figure 13. Radial profiles of (a) the perpendicular velocity u_{\perp} and its radial shear (dashed), (b) time delay of the cross-correlation τ_{max} , (c) tilt angle of the turbulence θ_{turb} and (d) correction factor F_d . Refer to the text for more details.

The increase of velocity shear towards the plasma edge agrees with the change of tilt angle to more positive values as predicted by equation (22). Hence at inner measurements positions with small velocity shear, the negative tilt angle might be a direct consequence of the mode structure. Nevertheless, since velocity shear changes rather slow in the radial range, the tilt change may alternatively indicate a potential large difference in the turbulence character or drive at different radial positions. Another element to be considered is the rational surface 8/5 at approximately $\rho \approx 0.75$, which may impact turbulence and heat transport [61]. The confirmation of the previous hypothesis requires further investigations, as the ongoing with gyrokinetic simulations for this specific discharge.

The two-point correlation technique has provided access to radially resolved measurements of the tilt angle. These and the simultaneously obtained flow measurements, provide important elements for investigating Reynolds stress and zonal flows [13].

6. Summary

A method for measuring the tilt angle of turbulent structures has been presented in detail. It uses the time delay of Doppler reflectometry channels probing at radially and perpendicularly displaced positions. The method has been deduced in slab geometry and for turbulence with a Gaussian wavenumber

spectrum. First, a point like and linear measurement has been assumed. Afterwards, diagnostic effects have been considered. It is shown that the method is also applicable when an extended scattering region and the k_{\perp} selectivity of the diagnostic are considered. Although contributions from forward scattering and direct reflection to the reflectometer signal may impact the correlation, they can be accounted for in the analysis and do not hinder the application of the method.

It has been shown that a finite decorrelation time τ_d of the turbulence may have an impact on the measured time delays for small velocities u_{\perp} . If the decorrelation time is shorter or comparable to the passing time of the structures in front of the probing beam, $\tau_d \leq w/u_{\perp}$, the time delays are underestimated and a correction factor F_d in the analysis is required. The relevance of this effect can be estimated for specific experimental conditions. Moreover assuming a Gaussian correlation function, a rough estimate of the decorrelation time has been obtained from F_d .

The method has been applied on L-mode discharges of the ASDEX Upgrade tokamak and of the TJ-II stellarator. The experimental time delays have been investigated and the tilt angle of turbulent structures has been measured in the core region of both devices, in TJ-II for the first time. In the ASDEX Upgrade tokamak, the method has been applied for two plasma discharges with different flow velocities u_{\perp} but the same reflectometer configuration. For high values of u_{\perp} , an accurate measurement of the tilt angle ($\theta_{\text{turb}} = 18 \pm 7^\circ$) is obtained and no F_d correction is needed. This measurement has been explained by the effect of the sheared $E \times B$ flow using linear ballooning theory. For low values of u_{\perp} , the temporal decorrelation of the turbulence affects the measurements and F_d is required. Furthermore a two-point correlation technique has been used to obtain a radial profile of the tilt angle, which is a first step towards Reynolds stress measurements.

The measurement method of the tilt angle provides a new tool for experimental investigations of turbulence in fusion plasmas. A proof of principle of its applicability has been provided in this paper. The novel measurements have been already compared with theory and simulations, and have demonstrated the effect of sheared $E \times B$ flows on structures in different turbulence regimes [28]. In the future, this method can be applied in other fusion machines where Doppler reflectometry is available, allowing for simultaneous studies of flow shear, tilt angle and turbulence decorrelation. This opens the door to advanced turbulence studies, for example of Reynolds stress and zonal flows, both important elements for understanding the turbulence dynamics in fusion plasmas.

Acknowledgments

This work was supported by the European Commission within the framework of the Erasmus Mundus International Doctoral College in Fusion Science and Engineering (FUSION-DC). This work has been carried out within the framework of the EUROfusion Consortium and has received funding from the Euratom research and training programme

2014–2018 and 2019–2020 under grant agreement No 633053. The views and opinions expressed herein do not necessarily reflect those of the European Commission.

This work was partially performed within the framework of the Helmholtz Virtual Institute on Plasma Dynamical Processes and Turbulence Studies using Advanced Microwave Diagnostics, and was partially funded by the Spanish Ministry of Science and Innovation under contract number FIS2017-88892-P.

Appendix. Effect of an extended scattering region and k_{\perp} selectivity

In this section, an extended scattering region and the k_{\perp} selectivity of Doppler reflectometry are considered for the slab case and in Born approximation. This is useful to assess the impact of the radial resolution δr and of the beam width w on tilt angle measurement method presented in section 2, and also to identify conditions for which it is accurate. Turbulence with Gaussian wavenumber spectrum is considered (see section 2), nevertheless this approach can be used to predict the diagnostic response for more general cases.

The Born approximation provides the reflectometer signal V when probing at the position (x, y) as [35, 36]

$$V(x, y) = \iint dx' dy' \delta n(x + x', y + y') W(x', y'), \quad (\text{A.1})$$

where the density fluctuation δn are weighted by W which corresponds to the square of the electric field of the wave, and is commonly referred to as the weighting function [62]. Normalization factors are excluded. The last expression considers the integration over the scattering volume, hence it is a generalization of the point measurement of equation (6).

For the sake of simplicity, W is approximated with a Gaussian

$$W(x, y) \approx \exp\left[-\frac{x^2}{(\delta r)^2} - \frac{2y^2}{w^2} - ik_{\perp}y\right], \quad (\text{A.2})$$

where δr is the radial resolution and w the beam width, both quantities determining the extension of the scattering region. The complex phase provides the k_{\perp} selectivity of the diagnostic. In Fourier space the filter function is

$$\widehat{W}^{-1}(k_x, k_y) = \exp\left[-\frac{k_x^2(\delta r)^2}{4} - \frac{w^2(k_y - k_{\perp})^2}{8}\right], \quad (\text{A.3})$$

where $\widehat{\cdot}^{-1}$ stands for the inverse Fourier transform. It corresponds to a 2D filter centred at $k_x = 0$ and $k_y = k_{\perp}$.

Writing δn in terms of the wavenumber spectrum from equations (4), (A.1) becomes:

$$V(x, y) = \iint dk_x dk_y h(k_x, k_y) \widehat{W}^{-1}(k_x, k_y) e^{ik_x x + ik_y y}, \quad (\text{A.4})$$

thus the signal is given by the turbulent field filtered in wavenumber space. This indicates the filtering role of a Doppler reflectometer.

The cross-correlation of the Doppler reflectometer signals is

$$\widetilde{C}_{\Delta x}(\Delta y) = \iint dx dy V^*(x, y) V(x + \Delta x, y + \Delta y),$$

where the tilde stands for the fact that the filtered signals are used as input. Inserting equation (A.4) in the last expression yields the correlation function

$$\widetilde{C}_{\Delta x}(\Delta y) = \iint dk_x dk_y |h(k_x, k_y)|^2 |\widehat{W}^{-1}(k_x, k_y)|^2 e^{ik_x \Delta x + ik_y \Delta y}. \quad (\text{A.5})$$

It corresponds to the inverse Fourier transform of the filtered k spectrum. This is different from the point measurement case of equation (9) where no filter is included.

For the Gaussian spectrum of equation (3), the integral in equation (A.5) is solved analytically obtaining

$$|\widetilde{C}_{\Delta x}(\Delta y)| = \exp\left[-\frac{(\Delta x)^2}{\widetilde{L}_x^2} - \frac{(\Delta y - \widetilde{m}\Delta x)^2}{\widetilde{L}_y^2}\right]. \quad (\text{A.6})$$

Only the absolute value is considered because the complex phase provides no further physical information. The tilded quantities are:

$$\widetilde{L}_x = L_x \sqrt{1 + \frac{2(\delta r)^2}{L_x^2}}, \quad (\text{A.7})$$

$$\widetilde{L}_y = \sqrt{L_y^2 + w^2 + \frac{2m^2(\delta r)^2}{1 + 2(\delta r)^2/L_x^2}}, \quad (\text{A.8})$$

$$\widetilde{m} = m \left(1 + \frac{2(\delta r)^2}{L_x^2}\right)^{-1}. \quad (\text{A.9})$$

It is important to note that no dependence with k_{\perp} is obtained for any of the quantities. This shows that for the turbulence model (see equation (3)) the k_{\perp} selectivity of the diagnostic has no impact on the tilt angle measurements. Nevertheless this could be a special condition for Gaussian spectra, further studies using equation (A.5) with more realistic wavenumber spectra, as for example those obtained from gyrokinetic simulations [9, 45], are left for the future.

Because of the finite radial resolution, the measured radial correlation length L_x is overestimated by a factor $\sqrt{1 + 2(\delta r)^2/L_x^2}$, and the slope m is underestimated by a factor $(1 + 2(\delta r)^2/L_x^2)^{-1}$. Nevertheless if the radial resolution is small compared to the radial correlation length, $\delta r \ll L_x$, this effect is small and the true L_x and m are recovered. Therefore the tilt angle measurement method is accurate under this condition.

The measured width of the correlation is overestimated by w and δr through the second and third term in equation (A.8), respectively. The beam width w , of the order of few cm, sets a minimum for \widetilde{L}_y . Furthermore w may dominate over the other terms defining to a large extent the width of the cross-correlation function: $\widetilde{L}_y \gtrsim w$.

ORCID iDs

J R Pinzón  <https://orcid.org/0000-0003-0621-5697>T Happel  <https://orcid.org/0000-0003-4364-9363>P Hennequin  <https://orcid.org/0000-0002-4848-4898>

References

- [1] Xanthopoulos P, Mynick H E, Helander P, Turkin Y, Plunk G G, Jenko F, Görler T, Told D, Bird T and Proll J H E 2014 Controlling turbulence in present and future stellarators *Phys. Rev. Lett.* **113** 155001
- [2] Brizard A J and Hahm T S 2007 Foundations of nonlinear gyrokinetic theory *Rev. Mod. Phys.* **79** 421–68
- [3] Garbet X, Idomura Y, Villard L and Watanabe T H 2010 Gyrokinetic simulations of turbulent transport *Nucl. Fusion* **50** 043002
- [4] Jenko F, Dorland W, Kotschenreuther M and Rogers B N 2000 Electron temperature gradient driven turbulence *Phys. Plasmas* **7** 1904–10
- [5] White A E *et al* 2008 Measurements of core electron temperature and density fluctuations in DIII-D and comparison to nonlinear gyrokinetic simulations *Phys. Plasmas* **15** 056116
- [6] Casati A *et al* 2009 Turbulence in the TORE SUPRA tokamak: measurements and validation of nonlinear simulations *Phys. Rev. Lett.* **102** 165005
- [7] Lin L, Porkolab M, Edlund E M, Rost J C, Fiore C L, Greenwald M, Lin Y, Mikkelsen D R, Tsujii N and Wukitch S J 2009 Studies of turbulence and transport in Alcator C-Mod H-mode plasmas with phase contrast imaging and comparisons with GYRO *Phys. Plasmas* **16** 012502
- [8] Stroth U *et al* 2015 Experimental turbulence studies for gyrokinetic code validation using advanced microwave diagnostics *Nucl. Fusion* **55** 083027
- [9] Happel T, Görler T, Hennequin P, Lechte C, Bernert M, Conway G D, Freethy S J, Honoré C, Pinzón J R, Stroth U and (the ASDEX Upgrade Team) 2017 Comparison of detailed experimental wavenumber spectra with gyrokinetic simulation aided by two-dimensional full-wave simulations *Plasma Phys. Control. Fusion* **59** 054009
- [10] Bañón Navarro A, Happel T, Görler T, Jenko F, Abiteboul J, Bustos A, Doerk H, Told D and (the ASDEX Upgrade Team) 2015 Gyrokinetic studies of core turbulence features in ASDEX upgrade H-mode plasmas *Phys. Plasmas* **22** 042513
- [11] Freethy S J, Görler T, Creely A J, Conway G D, Denk S S, Happel T, Koenen C, Hennequin P and White A E 2018 Validation of gyrokinetic simulations with measurements of electron temperature fluctuations and density-temperature phase angles on ASDEX Upgrade *Phys. Plasmas* **25** 055903
- [12] Manz P, Ramisch M and Stroth U 2009 Physical mechanism behind zonal-flow generation in drift-wave turbulence *Phys. Rev. Lett.* **103** 165004
- [13] Stroth U, Manz P and Ramisch M 2011 On the interaction of turbulence and flows in toroidal plasmas *Plasma Phys. Control. Fusion* **53** 024006
- [14] Fedorczak N, Ghendrih P, Hennequin P, Tynan G R, Diamond P H and Manz P 2013 Dynamics of tilted eddies in a transversal flow at the edge of tokamak plasmas and the consequences for L-H transition *Plasma Phys. Control. Fusion* **55** 124024
- [15] Diamond P H, Itoh S-I, Itoh K and Hahm T S 2005 Zonal flows in plasma—a review *Plasma Phys. Control. Fusion* **47** R35
- [16] Fedorczak N, Diamond P H, Tynan G and Manz P 2012 Shear-induced Reynolds stress at the edge of L-mode tokamak plasmas *Nucl. Fusion* **52** 103013
- [17] Kishimoto Y, Kim J-Y, Horton W, Tajima T, LeBrun M J and Shirai H 1999 Toroidal mode structure in weak and reversed magnetic shear plasmas and its role in the internal transport barrier *Plasma Phys. Control. Fusion* **41** A663
- [18] Biglari H, Diamond P H and Terry P W 1990 Influence of sheared poloidal rotation on edge turbulence *Phys. Fluids B* **2** 1–4
- [19] Kim J Y, Kishimoto Y, Wakatani M and Tajima T 1996 Poloidal shear flow effect on toroidal ion temperature gradient mode: a theory and simulation *Phys. Plasmas* **3** 3689–95
- [20] Camenen Y, Idomura Y, Jolliet S and Peeters A G 2011 Consequences of profile shearing on toroidal momentum transport *Nucl. Fusion* **51** 073039
- [21] Angioni C *et al* 2011 Intrinsic toroidal rotation, density peaking, and turbulence regimes in the core of tokamak plasmas *Phys. Rev. Lett.* **107** 215003
- [22] Shesterikov I, Xu Y, Tynan G R, Diamond P H, Jachmich S, Dumortier P, Vergote M, Van Schoor M, Van Oost G and (TEXTOR Team) 2013 Experimental evidence for the intimate interaction among sheared flows, eddy structures, reynolds stress, and zonal flows across a transition to improved confinement *Phys. Rev. Lett.* **111** 055006
- [23] Zweben S J, Stotler D P, Scotti F and Myra J R 2017 Two-dimensional turbulence cross-correlation functions in the edge of NSTX *Phys. Plasmas* **24** 102509
- [24] Carter T A and Maggs J E 2009 Modifications of turbulence and turbulent transport associated with a bias-induced confinement transition in the large plasma device *Phys. Plasmas* **16** 012304
- [25] Schaffner D A, Carter T A, Rossi G D, Guice D S, Maggs J E, Vincena S and Friedman B 2013 Turbulence and transport suppression scaling with flow shear on the large plasma device *Phys. Plasmas* **20** 055907
- [26] Guszejnov D, Bencze A, Zoletnik S and Krämer-Flecken A 2013 Determination of structure tilting in magnetized plasmas—Time delay estimation in two dimensions *Phys. Plasmas* **20** 062303
- [27] Fox M F J, van Wyk F, Field A R, Ghim Y C, Parra F I and Schekochihin A A 2017 Symmetry breaking in MAST plasma turbulence due to toroidal flow shear *Plasma Phys. Control. Fusion* **59** 034002
- [28] Pinzón J R, Happel T, Hennequin P, Angioni C, Estrada T, Lebschy A, Stroth U and (the ASDEX Upgrade Team) 2019 Experimental investigation of the tilt angle of turbulent structures in the core of fusion plasmas *Nucl. Fusion* **59** 074002
- [29] Hirsch M, Holzhauser E, Baldzuhn J, Kurzan B and Scott B 2001 Doppler reflectometry for the investigation of propagating density perturbations *Plasma Phys. Control. Fusion* **43** 1641
- [30] Hennequin P, Honoré C, Truc A, Quéméneur A, Fenzi-Bonizec C, Bourdelle C, Garbet X, Hoang G T and (the Tore Supra team) 2006 Fluctuation spectra and velocity profile from Doppler backscattering on Tore Supra *Nucl. Fusion* **46** S771
- [31] Happel T, Estrada T, Blanco E, Tribaldos V, Cappa A and Bustos A 2009 Doppler reflectometer system in the stellarator TJ-II *Rev. Sci. Instrum.* **80** 073502
- [32] Hillesheim J C, Peebles W A, Rhodes T L, Schmitz L, Carter T A, Gourdain P-A and Wang G 2009 A multichannel, frequency-modulated, tunable Doppler backscattering and reflectometry system *Rev. Sci. Instrum.* **80** 083507
- [33] Tokuzawa T, Ejiri A, Kawahata K, Tanaka K, Yamada I, Yoshinuma M, Ida K and Suzuki C 2012 Microwave

- Doppler reflectometer system in LHD *Rev. Sci. Instrum.* **83** 10E322
- [34] Molina Cabrera P, Coda S, Porte L, Offeddu N, Lavanchy P, Silva M and Toussaint M 2018 V-band Doppler backscattering diagnostic in the TCV tokamak *Rev. Sci. Instrum.* **89** 083503
- [35] Piliya A D and Popov A Y 2002 On application of the reciprocity theorem to calculation of a microwave radiation signal in inhomogeneous hot magnetized plasmas *Plasma Phys. Control. Fusion* **44** 467
- [36] Gusakov E Z and Popov A Y 2002 Non-linear theory of fluctuation reflectometry *Plasma Phys. Control. Fusion* **44** 2327
- [37] Pinzón J R, Happel T, Blanco E, Conway G D, Estrada T and Stroth U 2017 Enhanced Doppler reflectometry power response: physical optics and 2D full wave modelling *Plasma Phys. Control. Fusion* **59** 035005
- [38] Schirmer J, Conway G D, Holzhauser E, Suttrop W, Zohm H and (the ASDEX Upgrade Team) 2007 Radial correlation length measurements on ASDEX Upgrade using correlation Doppler reflectometry *Plasma Phys. Control. Fusion* **49** 1019
- [39] Fernández-Marina F, Estrada T and Blanco E 2014 Turbulence radial correlation length measurements using Doppler reflectometry in TJ-II *Nucl. Fusion* **54** 072001
- [40] Altukhov A B *et al* 2016 Poloidal inhomogeneity of turbulence in the FT-2 tokamak by radial correlation Doppler reflectometry and gyrokinetic modelling *Plasma Phys. Control. Fusion* **58** 105004
- [41] Gusakov E, Irzak M and Popov A 2014 Radial correlation reflectometry at oblique probing wave incidence (linear scattering theory predictions) *Plasma Phys. Control. Fusion* **56** 025009
- [42] Blanco E and Estrada T 2013 Two-dimensional full-wave simulations of radial correlation Doppler reflectometry in linear and non-linear regimes *Plasma Phys. Control. Fusion* **55** 125006
- [43] Sarazin Y *et al* 2011 Predictions on heat transport and plasma rotation from global gyrokinetic simulations *Nucl. Fusion* **51** 103023
- [44] Liewer P C 1985 Measurements of microturbulence in tokamaks and comparisons with theories of turbulence and anomalous transport *Nucl. Fusion* **25** 543
- [45] Görler T and Jenko F 2008 Multiscale features of density and frequency spectra from nonlinear gyrokinetics *Phys. Plasmas* **15** 102508
- [46] Happel T, Estrada T, Blanco E, Hidalgo C, Conway G D, Stroth U and (the TJ-II Team) 2011 Scale-selective turbulence reduction in H-mode plasmas in the TJ-II stellarator *Phys. Plasmas* **18** 102302
- [47] Prisiazhniuk D, Krämer-Flecken A, Conway G D, Happel T, Lebschy A, Manz P, Nikolaeva V, Stroth U and (the ASDEX Upgrade Team) 2017 Magnetic field pitch angle and perpendicular velocity measurements from multi-point time-delay estimation of poloidal correlation reflectometry *Plasma Phys. Control. Fusion* **59** 025013
- [48] Maggs J E and Morales G J 2011 Generality of deterministic chaos, exponential spectra, and lorentzian pulses in magnetically confined plasmas *Phys. Rev. Lett.* **107** 185003
- [49] Prisiazhniuk D 2017 Development and application of poloidal correlation reflectometry to study turbulent structures in the ASDEX Upgrade tokamak *PhD Thesis* Technische Universität München, Germany
- [50] Hennequin P, Honoré C, Quéméneur A, Truc A, Gervais F, Fenzi C and Sabot R 1999 Analysis of density fluctuation frequency spectra in Tore Supra as a tool for studying plasma motion and transport properties *Proc. 26th EPS Conf. on Plasma Physics*
- [51] Murmann H, Götsch S, Röhr H, Salzmann H and Steuer K H 1992 The Thomson scattering systems of the ASDEX Upgrade tokamak *Rev. Sci. Instrum.* **63** 4941–3
- [52] Fischer R, Wolfrum E, Schweinzer J and (the ASDEX Upgrade Team) 2008 Probabilistic lithium beam data analysis *Plasma Phys. Control. Fusion* **50** 085009
- [53] Poli É *et al* 2018 Torbeam 2.0, a paraxial beam tracing code for electron-cyclotron beams in fusion plasmas for extended physics applications *Comput. Phys. Commun.* **225** 36–46
- [54] Happel T, Conway G D, Kasperek W, Plaum B, Lechte C, Wagner D, Stroth U and (the ASDEX Upgrade Team) 2011 Design of a new Doppler reflectometer frontend for the ASDEX Upgrade tokamak *Proc. 10th Int. Reflectometry Workshop (Padual, Italy)*
- [55] Sabot R, Hennequin P and Colas L 2009 Fluctuation measurements and their link with transport on tore supra *Fusion Sci. Technol.* **56** 1253–72
- [56] Lebschy A *et al* (the ASDEX Upgrade Team) 2018 Measurement of the complete core plasma flow across the LOC-SOC transition at ASDEX Upgrade *Nucl. Fusion* **58** 026013
- [57] Peeters A G, Camenen Y, Casson F J, Hornsby W A, Snodin A P, Srintzi D and Szepesi G 2009 The nonlinear gyro-kinetic flux tube code GKW *Comput. Phys. Commun.* **180** 2650–72
- [58] Sánchez E, Estrada T, Velasco J L, Calvo I, Cappa A, Alonso A, García-Regaña J M, Kleiber R and Riemann J 2019 Validation of global gyrokinetic simulations in stellarator configurations *Nucl. Fusion* **59** 076029
- [59] van Milligen B P, Estrada T, Ascasíbar E, Tafalla D, López-Bruna D, López Fraguas A, Jiménez J A, García-Cortés I, Dinklage A and Fischer R 2011 Integrated data analysis at TJ-II: the density profile *Rev. Sci. Instrum.* **82** 073503
- [60] Castejón F, Cappa A, Tereshchenko M and Fernandez A 2008 Computation of EBW heating in the TJ-II stellarator *Nucl. Fusion* **48** 075011
- [61] van Milligen B P, Nicolau J H, García L, Carreras B A and Hidalgo C 2017 The impact of rational surfaces on radial heat transport in TJ-II *Nucl. Fusion* **57** 056028
- [62] Bulanin V V and Yafanov M V 2006 Spatial and spectral resolution of the plasma Doppler reflectometry *Plasma Phys. Rep.* **32** 47–55